A Method to Control the Environmental Wind Profile in Idealized Simulations of Deep Convection with Surface Friction

DANIEL T. DAWSON II

Department of Earth, Atmospheric, and Planetary Sciences, Purdue University, West Lafayette, Indiana

BRETT ROBERTS[a] AND MING XUE

Center for Analysis and Prediction of Storms, and School of Meteorology, University of Oklahoma, Norman, Oklahoma

(Manuscript received 31 December 2018, in final form 24 July 2019)

ABSTRACT

In idealized, horizontally homogeneous, cloud model simulations of convective storms, the action of surface friction can substantially modify the near-ground environmental wind profile over time owing to the lack of a large-scale pressure gradient force to balance the frictional force together with the Coriolis force. This situation is undesirable for many applications where the impact of an unchanging environmental low-level wind shear on the simulated storm behavior is the focus of investigation, as it introduces additional variability in the experiment and accordingly complicates interpretation of the results. Partly for this reason, many researchers have opted to perform simulations with free-slip lower boundary conditions, which with appropriate boundary conditions allows for more precise control of the large-scale environmental wind profile. Yet, some recent studies have advocated important roles of surface friction in storm dynamics. Here, a simple method is introduced to effectively maintain any chosen environmental wind profile in idealized storm simulations in the presence of surface friction and both resolved and subgrid-scale turbulent mixing. The method is demonstrated through comparisons of simulations of a tornadic supercell with and without surface friction and with or without invoking the new method. The method is compared with similar techniques in the literature and potential extensions and other applications are discussed.

1. Introduction

Idealized numerical modeling studies of convective storms have yielded many valuable insights into their behavior over the past few decades. The idealized modeling approach typically initializes a horizontally homogeneous ''storm environment'' that is defined by a single vertical profile (usually taken from a real-world sounding, extracted from NWP model output, or from analytical functions). This environment is assumed to be representative of large-scale (i.e., mesoalpha to synoptic) conditions and is usually, but not always, assumed to be invariant in time (so that storm behavior within a given fixed environment can be studied). Convective development is then encouraged through a variety of artificial forcing mechanisms such as thermal bubbles (Klemp and Wilhelmson 1978), imposed low-level convergence (Loftus et al. 2008), and updraft nudging (Naylor and Gilmore 2012). These simplifications are reasonable if the simulation domain is on the order of 100 km in width and the simulation length is on the order of a few hours. They allow for precise control over the background environment, and thus better understanding of how different environments (in particular the vertical structure of the environment) modulate the simulated storm characteristics. Most studies of this type represent any forces operating on these large scales either by neglecting them entirely or by prescribing some initial balance condition: typically geostrophic balance.

If we examine the horizontal momentum equations as applied to the *horizontally homogeneous large-scale environment* (hereafter simply ''environment'') of an idealized storm simulation, it is clear that the horizontal pressure gradient force (PGF) terms are identically

[a] Current affiliation: Cooperative Institute for Mesoscale Meteorological Studies, and NOAA/NWS/Storm Prediction Center, and NOAA/OAR/National Severe Storms Laboratory, Norman, Oklahoma.

Corresponding author: Daniel T. Dawson II, dandawson@purdue.edu

DOI: 10.1175/MWR-D-18-0462.1

zero, since by definition they depend on (large scale) horizontal gradients in pressure. However, the PGF is obviously important since, for example, it balances the Coriolis force under the assumption of geostrophic balance. Therefore the large-scale PGF must somehow be specified and *decoupled* from the actual model pressure field. We can then write the horizontal momentum equations for the evolution of this large-scale environment as follows:

$$\frac{\partial U}{\partial t} = \mathrm{PPGF}_x + fV + F_x[U, V]$$
$$\frac{\partial V}{\partial t} = \mathrm{PPGF}_y - fU + F_y[U, V], \quad (1)$$

where U and V are the horizontal wind components of the *horizontally homogeneous large-scale environment* (i.e., sans storm-induced perturbations), and PPGF_x and PPGF_y are the horizontal components of the *prescribed* large-scale "Pseudo-PGF" (hereafter just PPGF). We use the term "Pseudo-PGF" in this paper because it does not correspond to any actual large-scale horizontal gradient of the predicted pressure field in the model. $F_x[U, V]$ and $F_y[U, V]$ are the horizontal components of the frictional force. These contain the parameterized subgrid-scale turbulence mixing, computational mixing/diffusion (and potentially imposed artificial mixing), and the surface drag that defines the vertical momentum flux at the surface. The wind components are shown in brackets in these terms to emphasize their use in the turbulent mixing and surface drag formulations.

If frictional effects are neglected, then the PPGF can simply be obtained from

$$\mathrm{PPGF}_x = -fV_g$$
$$\mathrm{PPGF}_y = fU_g, \quad (2)$$

where U_g and V_g are the geostrophic wind components, usually assumed to be constant in time. The environmental horizontal momentum equations then become

$$\frac{\partial U}{\partial t} = f(V - V_g)$$
$$\frac{\partial V}{\partial t} = -f(U - U_g). \quad (3)$$

Thus, the PPGF is specified in this case by the constraint of geostrophic balance. A standard method in most idealized cloud models is to define the model *base state* using the geostrophic initial environment as defined here. Then, $(U, V) = (U_g, V_g)$ and from (3) the environmental horizontal winds remain steady in time, as desired. Otherwise, it is easy to see from (3) that this is mathematically equivalent to applying the Coriolis force only to the *perturbation* winds relative to this initial environment. Generalizing (3) to include horizontally varying perturbation winds, this is a standard run-time option for most models when run in "idealized cloud model mode".

In addition to the PPGF and the Coriolis force, friction is another force that is active at large scales. It is most important in the boundary layer, and particularly near the surface where the momentum flux from the surface dominates. In theory, when observed soundings are used to define the environment in idealized storm simulations, they should already be subject to the effects of friction. Under the aforementioned assumption of geostrophic balance (or no large-scale forces at all), however, the introduction of surface friction tends to modify the specified environmental sounding during the simulation (especially in the low levels), by reducing the near-surface wind speed (Adlerman and Droegemeier 2002; Wicker and Wilhelmson 1993). That is, the rhs of (1) now contains nonzero friction terms and the large-scale balance is upset. This problem has historically made it difficult to control the environmental wind profile while simultaneously incorporating the effects of surface friction through, for example, a drag parameterization or other imposition of no-slip or semislip lower boundary conditions. At least partly for this reason, the vast majority of idealized modeling studies have elected to use free-slip lower boundary conditions, thereby ignoring the direct effects of surface friction entirely.

However, it has long been recognized that the effects of surface friction are important for some aspects of severe convective storm behavior; a prime example is its role in tornado dynamics. Surface friction plays an important role in tornado structure and evolution through the formation of intense radial inflow in a shallow surface layer and subsequent rapid upward turning in the corner flow region (e.g., Lewellen and Lewellen 2007; Fiedler and Rotunno 1986; Davies-Jones 2014). Recent studies (Schenkman et al. 2014; Roberts et al. 2016; Markowski 2016; Mashiko 2016; Roberts and Xue 2017) have additionally found that surface friction may be implicated in processes leading to supercell tornadogenesis including as a potential direct source of horizontal vorticity that can be tilted into the vertical within the developing tornado. These reasons, among others, have motivated researchers to develop methods to incorporate the effects of surface friction while maintaining a specified low-level wind profile in simulations that include the tornado and its parent storm within the context of an idealized environment of the type discussed above.

Previous efforts to incorporate surface friction into idealized storm simulations have varied in their approach. Wicker and Wilhelmson (1993) were among the

first to study the effects of surface friction on the development of a simulated tornado within the context of a full 3D supercell simulation. In their doubly nested grid approach, they applied surface friction to a restart of their inner (120-m grid spacing) tornado-resolving grid, 900 s before tornadogenesis in the original, free-slip inner domain simulation. The outer grid (600-m grid spacing) maintained a free-slip lower boundary condition throughout the simulation period. In this manner, they were able to show that their simulated tornado responded to the presence of surface friction by contracting in radius and intensifying. In their case, the nested simulation after the introduction of friction was likely too short for significant changes to occur in the environmental wind profile, which was additionally maintained by the lateral boundary conditions from the no-friction outer grid.

Other studies have attempted to remove or mitigate the modification of the environmental wind profile due to the action of surface friction through various approaches. Wilhelmson and Chen (1982, hereafter WC82) modified the surface drag formulation such that it was only applied to the perturbation wind (relative to the initial environmental wind profile). Adlerman and Droegemeier (2002) used the WC82 method in their idealized supercell simulations to study the effects of surface drag with different specified magnitudes of the drag coefficient on the behavior of the simulated mesocyclones. More recently, Roberts et al. (2016, hereafter R16) and Markowski (2016, hereafter M16) independently developed different methods by which surface drag could be incorporated into an idealized simulation framework while simultaneously maintaining a more-or-less unchanged environmental wind profile throughout a simulation. Coffer and Parker (2017) applied the R16 method to their idealized simulations of supercells in nontornadic and tornadic environments derived from composites of VORTEX-2 proximity soundings (Parker 2014).

The WC82, R16, and M16 methods can be cast within the context of a more general framework where friction is included in an (up to) three-way balance with the Coriolis and the PPGF. Johnson (1966) proposed the term *geotriptic* for this three-force balance (where, in addition to the surface friction itself, the internal turbulent eddy flux is also balanced).

The rest of this paper is organized as follows: in section 2, we discuss these previous methods, introduce a new method that overcomes some of their limitations, and describe its implementation into a numerical cloud model. In section 3, we test the new method with simulations of a supercell in an environment derived from the 24 May 2011 Oklahoma tornado outbreak. The simulations compare traditional free-slip simulations with the new method, with the WC82 base state surface drag removal method, and with unbalanced surface drag. Section 3 also describes the results of corresponding simulations in which the prestorm environment includes resolved turbulent eddies. Section 4 describes and compares the structure and behavior of the simulated storm across the simulations, focusing on the structure of surface boundaries. Finally, section 5 summarizes the paper and discusses some potential modifications to the method and broader applications.

2. Description of the new method

a. Description of previous methods

As stated previously, it is difficult to include the effects of surface friction but also maintain a specified wind profile in idealized storm simulations. R16 addressed this problem by first running a 1D column simulation (representing the horizontally homogeneous environment) with the same vertical grid spacing, surface drag coefficient, and turbulence parameterization as in their fully 3D runs. They assumed an initial *geostrophic balance*. Thus, in their 1D simulation the only forces acting on the wind components were the PPGF (specified via the assumption of initial geostrophic balance), the Coriolis force and friction:

$$\frac{\partial U}{\partial t} = f(V - V_g) + F_x[U, V]$$
$$\frac{\partial V}{\partial t} = -f(U - U_g) + F_y[U, V]. \quad (4)$$

During the column simulation these three forces together slowly modified the wind profile, eventually reaching a steady state in approximate *geotriptic balance*. R16 then used this final balanced wind profile to initialize the environment of their 3D simulations; as such, the wind profile would remain in a quasi-steady state away from storm-induced perturbations.

Similar to R16, though not running a completely separate simulation, M16 sought a balanced wind profile by first allowing friction to modify the wind profile in their ''toy model'' supercell tornado simulations prior to the activation of the artificial heat source to initiate convection. Then after the first hour of this ''adjustment'' period, they applied a nudging term to the model horizontal momentum equations that slowly relaxed the horizontal mean wind profile back toward the mean profile as it was at 1 h simulation time. The wind profile reached a near–steady state by 2 h, at which point they

activated their heat source to generate the "toy" supercell. Moreover, they excluded the Coriolis force from their simulations entirely; the nudging terms thus "crudely mimic the influence of a large-scale horizontal pressure-gradient force and Coriolis force" (M16). The relaxation coefficient was chosen to minimize the impact on the storm-induced perturbations while still maintaining a constant "far-field" environmental wind profile.

Finally, instead of assuming an initial *geostrophic* balance as in R16, WC82 assumed that the surface drag was *already* in balance with an assumed PPGF (and possibly also Coriolis force, if it is active in the simulation). In a manner reminiscent of modifying the Coriolis term in (3) via the geostrophic balance relations (2), WC82 modified the surface drag formulation so that the drag was only applied to the perturbation wind relative to the initial environmental wind profile.

b. Description of the new method

The WC82, M16, and R16 methods can each be viewed ultimately as methods to compute or specify a PPGF that is consistent with a large-scale three-way balance between the PPGF, Coriolis, and friction forces. Inspired by these previous efforts and in an attempt to overcome some of their limitations, we propose a new method to determine the PPGF based on a three-term balance equation (hereafter the "Geotriptic Wind Balance", or GWB method). The PPGF can be specified through the geotriptic wind balance relation:

$$\begin{aligned} \mathrm{PPGF}_x &= -fV - F_x[U,V] \\ \mathrm{PPGF}_y &= fU - F_y[U,V]. \end{aligned} \tag{5}$$

One may then compute the needed PPGF with knowledge of the large scale Coriolis and frictional forces in the model. Our method for doing so has a similar starting point to R16 and M16 in that we leverage the model integration sans any storm-induced perturbations. Specifically, we use the model state prior to the introduction of artificial forcing at or near the beginning of the simulation. Instead of computing the PPGF from (2) and running out to a steady state as in R16, we initially assume it to be zero, such that the (imbalanced) Coriolis and friction forces are the only ones acting on the wind profile:

$$\begin{aligned} \frac{\partial U}{\partial t} &= fV + F_x[U,V] \\ \frac{\partial V}{\partial t} &= -fU + F_y[U,V]. \end{aligned} \tag{6}$$

Combining (5) and (6) we see that the required PPGF for geotriptic balance is simply the *negative* of the time tendency of the horizontal wind components, which can be estimated from their change after the first time step of model integration:

$$\begin{aligned} \mathrm{PPGF}_x &= -fV - F_x[U,V] = -\frac{\partial U}{\partial t} \approx -\frac{U_f - U_i}{\Delta t} \\ \mathrm{PPGF}_y &= fU - F_y[U,V] = -\frac{\partial V}{\partial t} \approx -\frac{V_f - V_i}{\Delta t}, \end{aligned} \tag{7}$$

where the subscripts for U and V indicate the initial and final values for each model time step, and Δt is the duration of the model time step. We calculate (7) at each vertical grid level in a column well removed from the initial storm-induced perturbations, or at each column in a given region and then taking a horizontal average. The result is the vertical PPGF profile that is then applied uniformly as an additional source term in the prognostic horizontal momentum equation at all grid columns for the remainder of the simulation. In practice we have found that the balance provided by this initial vertical PPGF profile is occasionally slightly upset during the first few minutes of model integration, possibly due to the effects of the initial development of subgrid-scale TKE. Testing (not shown) has revealed that continuously updating the PPGF profile after each time step for the first 300 s or so is sufficient to compensate for this effect. That is, after each time step for the first 300 s, we compute the new PPGF as follows:

$$\mathrm{PPGF}_{(x,y)}(t_f) = \mathrm{PPGF}_{(x,y)}(t_i) - \frac{(U,V)_f - (U,V)_i}{\Delta t}, \tag{8}$$

where the last term on the rhs now represents the residual u- or v-momentum time-tendency not accounted for by the PPGF computed in the previous time step. Before the calculation of the PPGF at the first time step, it is initialized to zero so that (7) is recovered. With the estimated PPGF included in the model, the wind profile is expected to remain quasi-steady in time away from storm-induced perturbations.

Whereas R16 finds an *adjusted* wind profile that is consistent with a geotriptic balance between the model friction force, the Coriolis, and a PPGF specified via an initial *geostrophic* balance, the GWB method works the other way and computes a PPGF that is in geotriptic balance with Coriolis and friction for a given *fixed* wind profile. At least for applications that require or benefit from control over the environmental wind profile, this ability to compute the necessary PPGF for geotriptic balance [via (5)] for any given initial wind profile is the new method's chief advantage over the R16 method. Moreover, the final adjusted wind profile in the R16 method will change as a function of details of the model friction

parameterization, such as the value of the surface drag coefficient, whereas in the GWB method, the computed PPGF will change instead to compensate and maintain the same wind profile. In this regard, the GWB method is similar to the WC82 method, in that both effectively find a PPGF that counteracts the effects of surface friction on the environmental wind profile while still incorporating its effects on storm-induced perturbations. The chief advantage of the GWB method over WC82 is that it additionally balances the effects of friction *above the surface*, which may be substantial in some cases.

Finally, both the GWB and M16 methods work by adding an additional forcing term to the rhs of the model momentum equations. In M16, the forcing term is a Newtonian relaxation (or nudging) term that increases in magnitude the more the horizontally averaged wind field differs from the reference profile. In contrast, in the simplest configuration of the GWB method (after the initial 300-s adjustment period) this term is constant in time and there is no forced relaxation toward a reference wind profile, which simplifies interpretation of the results. In this regard, our method is reminiscent of that of Nowotarski et al. (2015) who also added artificial forcing terms to the model momentum equations (as well as the potential temperature and water vapor conservation equations). The forcing terms in their study were also only a function of height and were computed from the horizontal and time-averaged change in these variables over a 2-h period in a separate "stormless" simulation that included the growth of a realistic convective boundary layer. The goals of Nowotarski et al. (2015) and the current study are different, however, as they were concerned with the evolution of simulated storms in an *evolving* environment, whereas we again are concerned with how to maintain a *fixed* environment for simulated storms while still accounting for the effects of surface friction. Nevertheless, we adopt a very similar approach to initialize our supercell simulations with a turbulent boundary layer, where we additionally make use of a time-varying PPGF (see section 3d).

3. Application of the GWB method to idealized supercell simulations

a. Overview

Next, we explore the utility of the GWB method through a series of idealized simulations of a strongly tornadic supercell and its environment using the Bryan Cloud Model, release 18.2 (CM1; Bryan and Fritsch 2002). We initialized the simulations using a sounding derived from the RUC model that was representative of the inflow environment of the tornadic supercells of the 24 May 2011 central Oklahoma tornado outbreak (Fig. 1; Orf et al. 2017; L. J. Wicker 2017, personal communication). The model domain is 200 × 200 × 20 km^3 with a horizontal grid spacing of 250 m in an inner 100 × 100 km^2 region (hereafter the "inner domain") and gradually stretched to 1 km at the lateral boundaries. The surrounding outer stretched region of grid points is intended to provide a larger area to minimize undesired lateral boundary condition effects, as well as to serve as a zone where turbulent eddies can be introduced (see section 3d) before entering the inner high-resolution domain. A stretched vertical grid is imposed with 53 levels with spacing from 20 m near the surface to 800 m at the model top. The domain translates with a constant $[u, v] = [14.2, 12.1]$ m s^{-1} to keep the simulated storm near the center of the domain (though the Coriolis and frictional forces still act on the original ground-relative winds). To initiate convection, we use the updraft nudging technique of Naylor and Gilmore (2012) within an ellipsoidal region of radii 10 km × 10 km × 1.5 km, centered at $x = 100$ km, $y = 100$ km, and $z = 1.5$ km. The maximum magnitude of the nudging is 10 m s^{-1} and is applied over the first 900 s of the model integration. We employed the triple-moment version of the NSSL microphysics scheme (Mansell 2010; Dawson et al. 2014) and a 1.5-order prognostic TKE subgrid turbulence closure method based on Deardorff (1980). All simulations included the horizontal components of the Coriolis force with a constant Coriolis parameter $f = 1 \times 10^{-4}$ s^{-1}. We divide our experiments into sets with the following naming convention: [S, NS]-[T, NT]-[D, ND]-[GEO, GWB, WC], where we apply all combinations of each term in brackets for a total of 20 simulations. We describe each of the terms in the brackets in Table 1 and in detail in the following sections.

b. Simulation of the environmental wind profile evolution in the absence of convection

We first performed a set of simulations with no initial updraft forcing ("no-storm" or NS) and without resolved turbulence in the boundary layer ("no-turbulence" or NT). The goal of these experiments is to test the GWB method in the absence of storm-induced perturbations. This series contained simulations with and without surface drag (D and ND, respectively), and with and without the GWB method applied: NS-NT-D-GEO, NS-NT-ND-GEO, NS-NT-D-GWB, and NS-NT-ND-GWB. Additionally, we performed a simulation with surface drag but applying the WC82 base-state drag subtraction method: NS-NT-D-WC. Each simulation was integrated for 4 h. In the experiments that included surface drag, it was parameterized

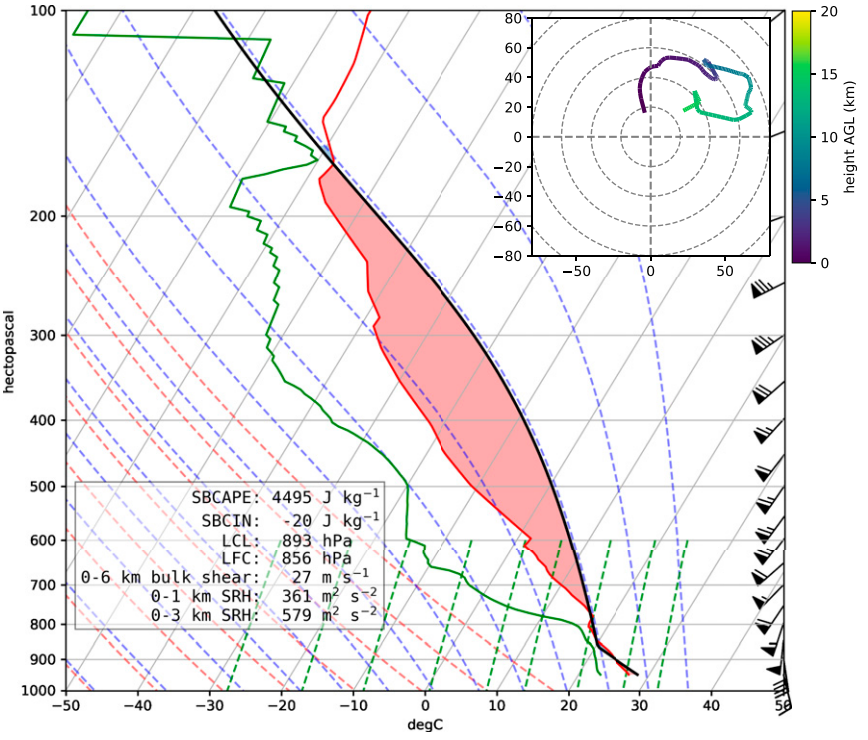

FIG. 1. Skew T–log$p$ and hodograph for the RUC-derived 24 May 2011 inflow sounding used in the simulation experiments.

by the introduction of horizontal momentum stresses at the ground level as in R16:

$$-\tau_{13}(z=0) = \rho C_d V_h u, \tag{9}$$

$$-\tau_{23}(z=0) = \rho C_d V_h v, \tag{10}$$

where τ_{13} and τ_{23} are the subgrid-scale stress tensor components associated with the turbulent flux of zonal u and meridional v (ground-relative) momentum, respectively; V_h is the ground-relative horizontal wind speed; and C_d is the dimensionless drag coefficient that is set to a constant value of 0.01 in each of the experiments with surface drag. For the GWB experiments, the PPGF profile was calculated using the gridcell area-weighted horizontal domain average of the time tendency of the horizontal momentum components. Again, the PPGF profile was updated each time step for the first 300 s of the simulation to account for the initial development of subgrid-scale turbulence and its early effect on the wind and thermodynamic profiles (not shown), and held fixed thereafter.

We show the temporal evolution of the low-level wind profile (horizontally averaged over the inner domain) for each of the NS-NT- experiments in Fig. 2. Turning to the experiments without surface drag first, NS-NT-ND-GEO (Fig. 2d) assumes an initial large-scale geostrophic balance [i.e. computes the PPGF using (2)], while the PPGF in NS-NT-ND-GWB (Fig. 2e) is computed from (5) and thus additionally accounts for the effects of internal mixing on the profile. NS-NT-ND-GEO shows only small changes in the wind profile over time, mainly in a slight reduction in the wind speed near the surface (see circles in Fig. 2d) and in a straightening of the

TABLE 1. Simulation configuration. Experiment naming key: S = storm, NS = no storm, T = resolved BL turbulence, NT = no resolved BL turbulence, D = surface drag, ND = no surface drag.

Experiment names	Description
[S, NS]-[T, NT]-ND-GEO	No surface drag with initial geostrophic balance using (2)
[S, NS]-[T, NT]-ND-GWB	No surface drag with GWB method applied
[S, NS]-[T, NT]-D-GEO	With surface drag and initial geostrophic balance
[S, NS]-[T, NT]-D-GWB	With surface drag with GWB method using (5)
[S, NS]-[T, NT]-D-WC	With surface drag, but with base-state surface drag removed (Wilhelmson and Chen 1982)

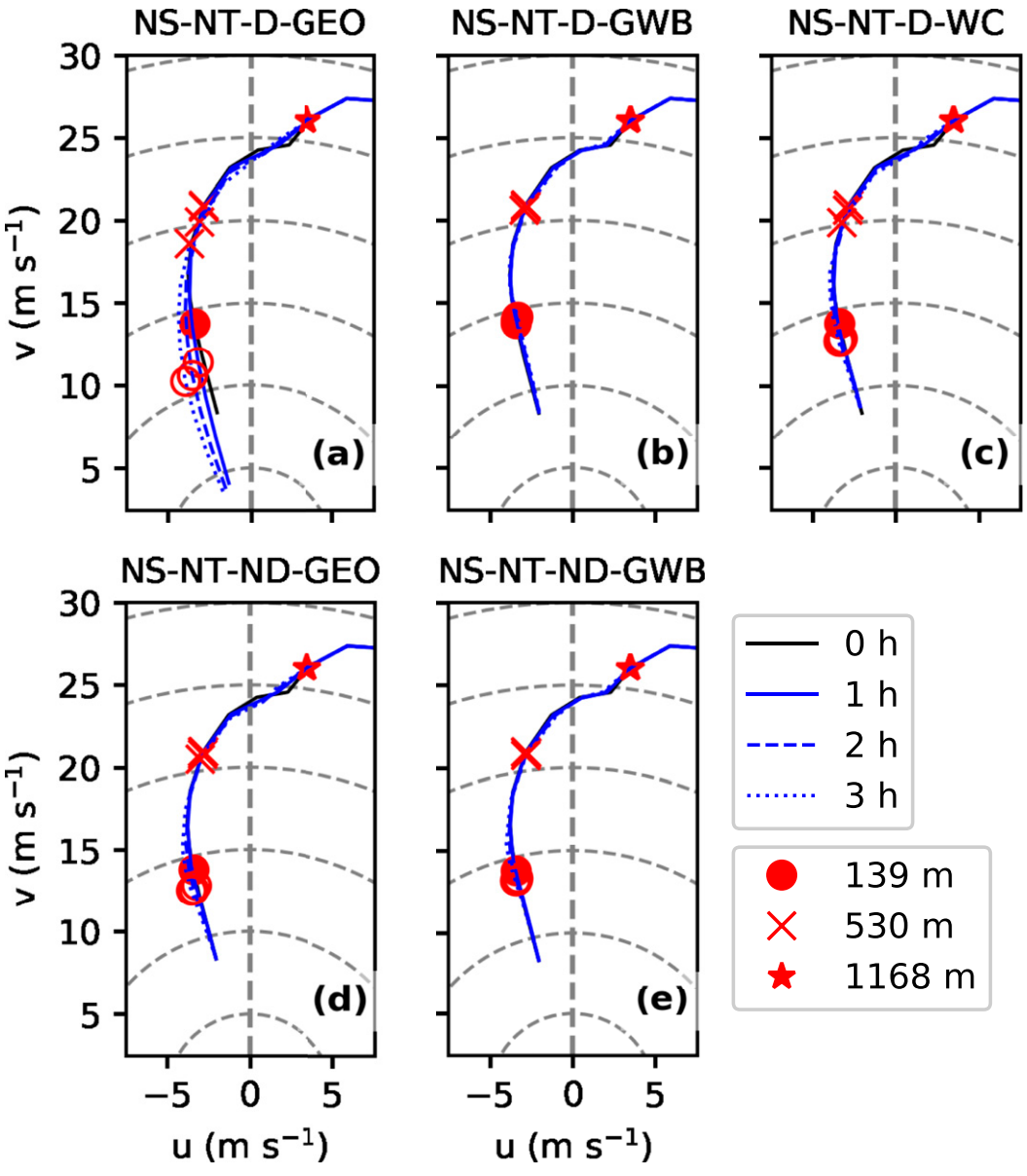

FIG. 2. Hodographs for each of the no-storm runs without resolved boundary layer turbulence (NS-NT-). For clarity, only the lower portions of the hodographs are plotted. The hodographs were computed from a weighted (by gridcell area) horizontal average of the entire domain. Initial hodographs are shown in black, while the 1-, 2-, and 3-h forecast times are shown in blue with changing line styles (see legend). Red markers (see legend) indicate specific heights (m AGL).

hodograph between 500 and 1000 m AGL (hodograph segment between × and star markers in Fig. 2d), while changes in NS-NT-ND-GWB are barely noticeable (Fig. 2e). The minor changes to the hodograph in NS-NT-ND-GEO reflect the subtle action of internal subgrid-scale turbulent mixing on the wind profile; the fact that these changes are relatively small confirms that the internal mixing by itself has minimal effect, at least for this particular wind profile and subgrid-scale turbulence parameterization.

The experiments with surface drag, in contrast, show substantial differences in the evolution of the near-surface wind profile. The hodograph evolution in NS-NT-D-GEO (Fig. 2a) differs substantially from that in NS-NT-D-GWB (Fig. 2b). The near-surface hodograph (i.e., below 1 km AGL) in NS-NT-D-GEO lengthens substantially over time owing to a reduction in the near-surface wind speed by the action of the surface drag. A similar effect is seen in the adjustment to the 3 May 1999 hodograph in R16 when they ran the original

wind profile through a 1-D simulation that creates a steady-state balanced sounding (their Fig. 1). It can be inferred that the wind profile that a simulated storm ''sees'' will differ in potentially important ways from the initial environment if friction is not included in the large-scale force balance with the PPGF computed appropriately. On the other hand, in NS-NT-D-GWB, the wind profile remains nearly constant in time, by design (Fig. 2b). Finally, the NS-NT-D-WC hodograph evolution is very similar to that of NS-NT-D-GWB, except again for a slight reduction in the wind speeds just above the surface (Fig. 2c, circles) and a straightening of the hodograph between 500 and 1000 m AGL (Fig. 2c, hodograph segment between × and star markers), This represents a slight weakening of the shear in the lowest couple hundred meters relative to the initial profile. This behavior is nearly identical to that in NS-NT-ND-GEO (Fig. 2d, circles) and is due to the WC82 method only ''balancing'' the effects of the drag at the first level above the surface; the GWB method computes a PPGF that also accounts for the effects of surface drag and turbulent mixing throughout the entire profile.

c. *Supercell storm simulations*

We then performed a corresponding set of simulations, this time with early updraft forcing included but again with no resolved boundary layer turbulence (the S-NT- simulations). The updraft forcing was applied starting at 300 s—just after the initial PPGF profile adjustment period to avoid contaminating the PPGF profile with the effects of storm-induced perturbations—and ending at 1200 s into the simulation. In each simulation, an intense supercell storm formed with a maximum updraft near 80 m s^{-1} (Fig. 3a) and persisted for 3+ h, producing multiple intense tornado-strength vortices with maximum surface vorticity and wind speeds exceeding 1 s^{-1} and 100 m s^{-1} in some cases (Figs. 3b and 3c, respectively). (Transient updrafts reaching 140+ m s^{-1} in Fig. 3a are associated with intensification of the vortices either at the surface or aloft). However, after 3 h, there was a tendency for the storm in each simulation to begin to lose supercell characteristics, as other cells that developed nearby began to merge their outflow with the primary cell, leading to upscale growth (not shown). For this reason we will only concern ourselves with the model output out to 3 h. As will be discussed in section 3d, the structure and behavior of the simulated storms, particularly near the surface, were substantially different between the simulations.

Similar to the NS-NT- experiments, we plot the hodograph evolution for the set of storm simulations in Fig. 4. In this case, however, we computed the hodographs from a horizontal average of the horizontal wind components in a 20 × 20 km^2 area at the southeast corner of the inner 250-m mesh, considered to be representative of the ''far-field'' inflow environment outside of the region most affected by storm-induced perturbations. If the GWB method is working well, we would expect this region far from the storm to show very limited modification over the period of the simulation similar to the corresponding ''no-storm'' case. As a comparison of Figs. 2 and 4 shows, there are still impacts from the storm visible in the far-field profile evolution, especially at the later times for S-NT-ND-GEO and S-NT-ND-GWB (Figs. 4d and 4e, respectively). Nevertheless, these are minor, and the GWB method clearly maintains a quasi-steady far-inflow wind profile for out to 3 h (Figs. 4b and 4e), as desired. The S-NT-D-WC experiment also exhibits a relatively steady wind profile (Fig. 4c), though not as steady as S-NT-D-GWB (Fig. 4b). The fact that the GWB method can preserve the initial wind profile with only limited modification in the *far inflow* environment while still allowing the environment closer to the storm to evolve appropriately is clearly an advantage for studies that wish to systematically investigate the behavior of storms in a prespecified/user-defined shear environment.

d. *Resolved versus subgrid-scale turbulence with the GWB method*

Markowski and Bryan (2016) compared LES-scale simulations of atmospheric boundary layers with and without resolved-scale turbulent structures. They demonstrated that when the initial environmental flow is laminar (i.e., does not contain appreciable turbulent structures that are resolved on the grid), common LES turbulent closure assumptions tend to overestimate the amount of shear in the surface layer. In their simulations where resolved turbulence was activated via the introduction of random perturbations to the initial state that were then recycled through the periodic boundaries, the near-surface shear was reduced, as was the fraction of TKE partitioned into the subgrid-scale parameterization. This issue potentially has implications for the interpretation of the effects of surface drag on a wide range of simulated storm behavior, and we refer the reader to Markowski and Bryan (2016) for details. For our purposes, when resolved turbulent structures are present in the prestorm boundary layer environment, the environmental wind profile is clearly no longer even approximately horizontally homogeneous. Yet, there still may be a desire to maintain the *horizontal mean* profile in the same way as when the prestorm environment is laminar. To demonstrate the utility of the GWB method for this

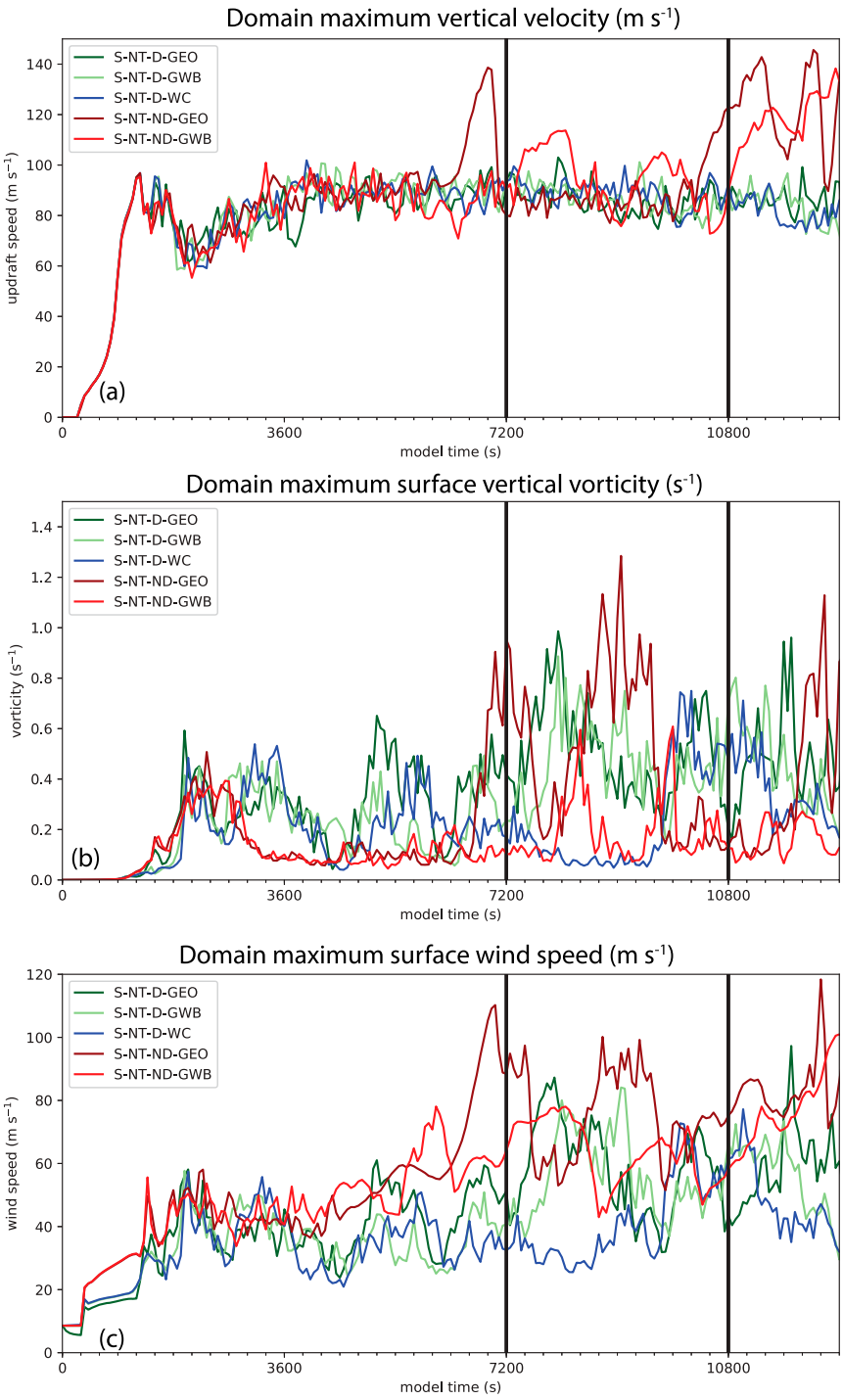

FIG. 3. Time series of domain maximum (a) vertical velocity ($m\,s^{-1}$), (b) surface vertical vorticity (s^{-1}), and (c) surface wind speed ($m\,s^{-1}$) for each of the storm simulations without resolved boundary layer turbulence (the S-NT- simulations). The black vertical lines denote the start and end times of the temporal composites described in section 4.

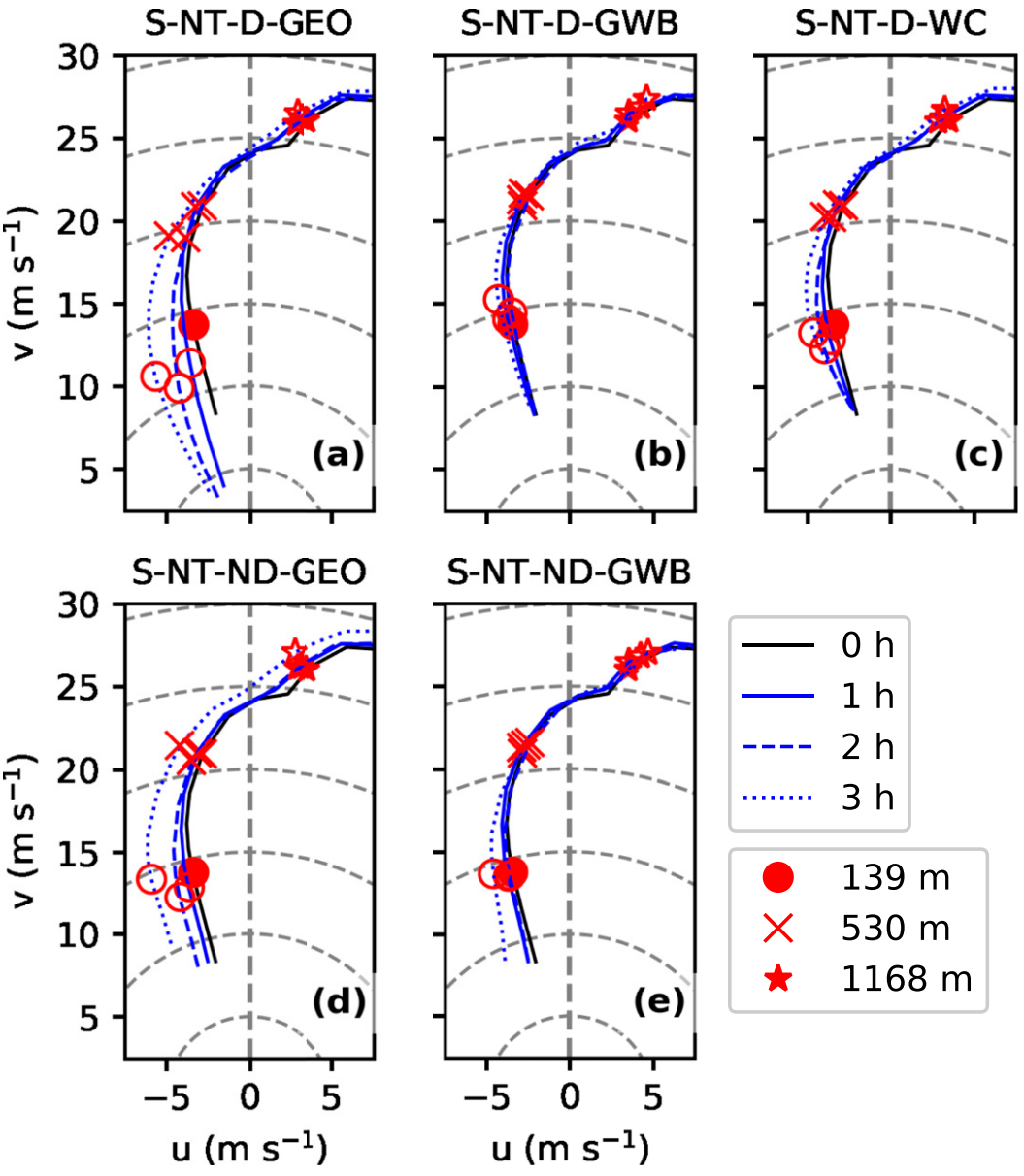

FIG. 4. As in Fig. 2, but for the storm simulations without resolved boundary layer turbulence (S-NT-).

situation, we perform and analyze two additional sets of experiments in which the boundary layer contains resolved turbulent structures.

We first discuss the NS-T- experiments–analogous to the NS-NT- experiments but including a field of resolved turbulent structures in the boundary layer. Our main purpose is to analyze the impact of resolved turbulence on the average environmental wind profile for the same experimental setup as the original NS-NT- experiments (i.e., without storm-induced perturbations). Our method for encouraging the development of turbulence is similar to the ''point'' method of Muñoz-Esparza et al. (2014). We apply random uniformly distributed potential temperature perturbations of ±0.25 K to the initial conditions, as well as every 200 s during the model integration to a 20-gridpoint-wide zone positioned 40 grid points from each inflow boundary. We apply the perturbations from the surface up to 1 km AGL, the approximate depth of the boundary layer in this case. This mechanism leads to well-developed turbulent structures in the boundary layer by approximately 1–2 h, which continue to grow in intensity until the end of the simulation (Fig. 5). That is, the turbulence never reaches a statistically steady state. We do not, however, consider this to be detrimental to our goal, which

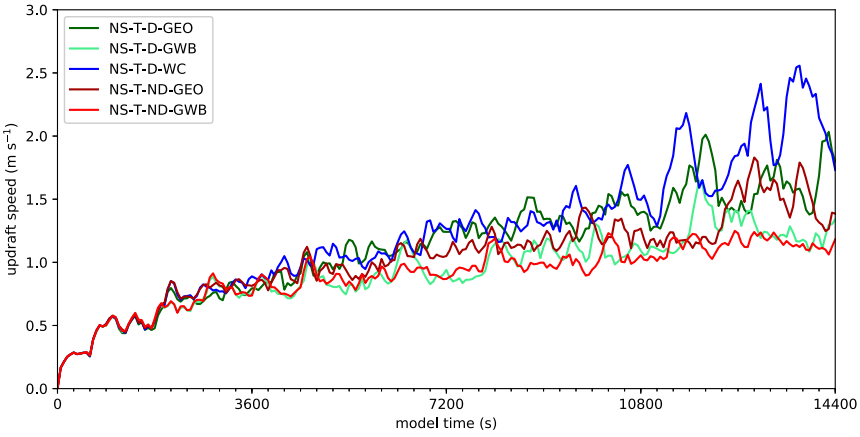

FIG. 5. As in Fig. 3a, but for the no-storm simulations with resolved boundary layer turbulence (NS-T-).

is to understand the impact on the wind profile in a qualitative sense. Future work may focus on developing a more robust methodology for generating a turbulent boundary layer in a statistically steady state with a given mean wind profile, perhaps by using an ''eddy injection'' method similar to Bryan et al. (2017). Because the resolved turbulence is changing in intensity with time, for the two experiments where we applied the GWB method—NS-D-GWBT- and NS-ND-GWBT—we update the PPGF profile every time step throughout the simulation, instead of only the first 300 s as in the NS-T- experiments. Again, we use the grid-area-weighted domain horizontal average of the horizontal momentum time tendencies to compute the PPGF profile, which effectively removes the effect of small-scale fluctuations owing to the turbulent eddies.

In Fig. 6, we show vertical profiles valid at 2 h of the subgrid-scale versus resolved turbulence kinetic energy (TKE), horizontally averaged over the inner domain, for each corresponding pair of experiments without (NS-NT-) and with (NS-T-) resolved boundary layer (BL) turbulence (left and right columns, respectively). Resolved TKE was computed according to $\mathrm{TKE} = 0.5\sqrt{u'^2 + v'^2 + w'^2}$, where the primes represent departures from the domain horizontal averages of each of the three wind components. Consistent with the results of Markowski and Bryan (2016), the NS-NT- experiments contain virtually no resolved TKE, while the NS-T- experiments have a substantial portion of the total TKE taken up by the resolved flow. For each of the experiments without parameterized surface drag (the -ND-GEO and -ND-GWB experiments), the surface layer exhibits relatively small magnitudes of either resolved or subgrid-scale TKE, as expected (Figs. 6g–j). In contrast, in the experiments with surface drag (-D-GEO, -D-WC and -D-GWB), the subgrid-scale TKE in the surface layer is much larger than anywhere else in the profile (Figs. 6c–f) owing to the large assumed surface drag-induced shear in the lowest 10 m (below the lowest height at which the model horizontal wind components are valid). It is this large surface layer subgrid-scale turbulence that is directly responsible for the rapid weakening of the near-surface winds in the experiments that included surface drag but only initial geostrophic balance (NS-NT-D-GEO and NS-T-D-GEO; cf. Fig. 2a and Fig. 7a). By 2 h, owing to these reduced surface winds, the amount of subgrid-scale turbulence in the surface layer is correspondingly reduced in both of these experiments (Fig. 6a) as compared to any of the experiments where the PPGF does not account for the surface drag (Figs. 6c–f).

When the GWB method is not active (i.e., in the GEO and WC experiments), the presence or absence of boundary layer turbulence has only modest effects on the overall evolution of the wind profile, despite the large differences in the vertical profiles of TKE between corresponding pairs (cf. left and right columns of Fig. 6). However, there is slightly more modification of the hodograph between ~500 and 1000 m in the non-GWB turbulent BL experiments (Figs. 7a,c,d) than in the corresponding non-turbulent BL experiments (Figs. 2a,c,d). This additional modification can be explained by the presence of substantial resolved TKE maximized near 500 m AGL in the turbulent-BL runs (Fig. 6 right column), but with the subgrid-scale TKE remaining nearly the same as in their nonturbulent BL counterparts (Fig. 6 left column).

When the GWB method is active and surface drag is present, the surface drag is offset by a strong PPGF (Fig. 8: red line near the surface). Above this shallow surface layer (or throughout the profile for the runs without surface drag; blue lines), the magnitude of the

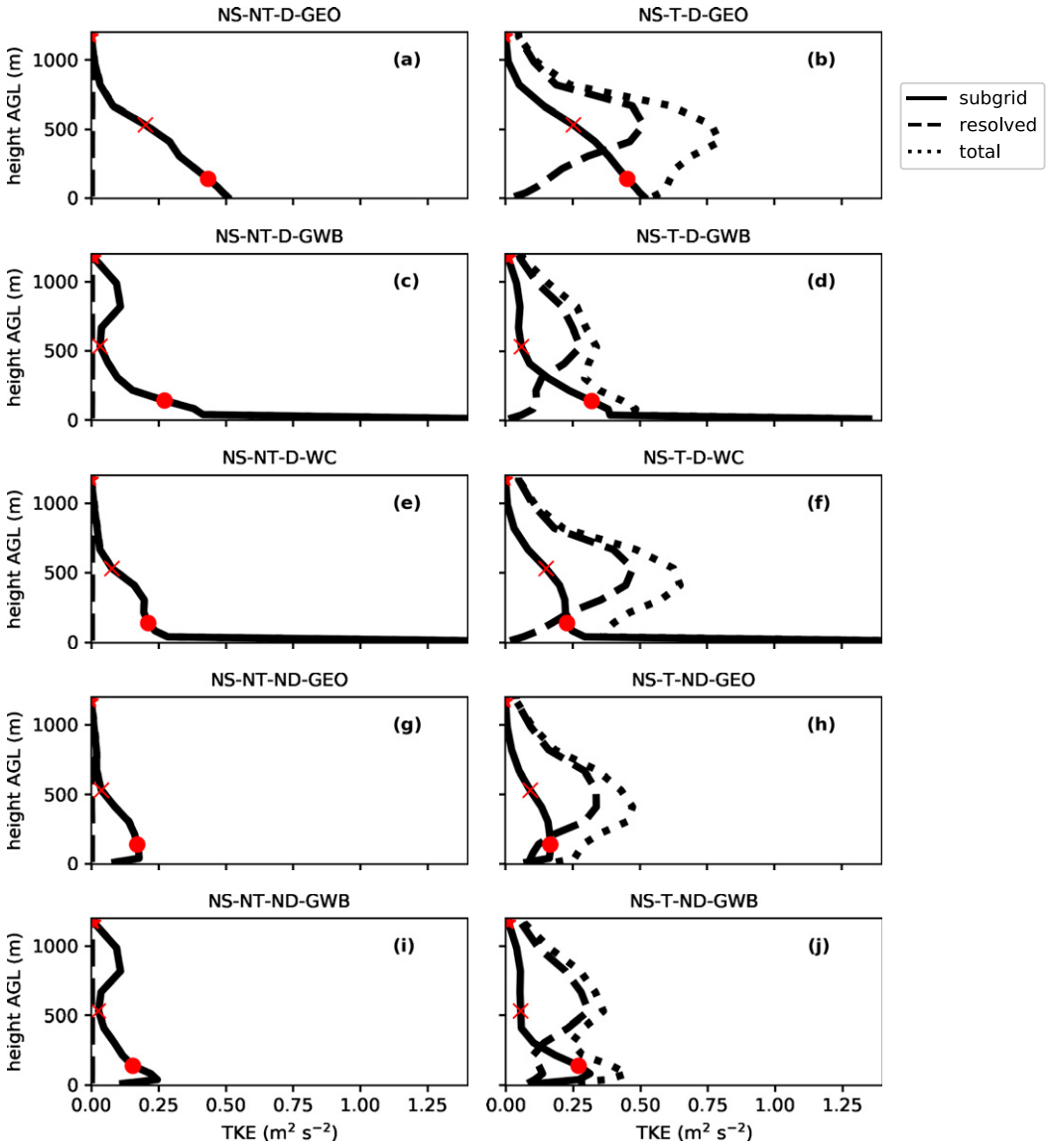

FIG. 6. Vertical profiles valid at 2 h of inner domain horizontal mean subgrid-scale (solid), resolved (dashed), and total (dotted) TKE for each of the (left) NS-NT- and (right) NS-T- simulations. Red markers indicate the same heights AGL as in Figs. 2 and 4.

PPGF is much lower and its profile differs between the turbulent and nonturbulent BL simulations (Fig. 8a). In particular, the turbulent-BL simulations show less southward-directed (or more northward-directed) PPGF in the turbulent runs (dashed lines) than the nonturbulent runs (solid lines), indicating a tendency for the resolved turbulent mixing in this portion of the profile to weaken the meridional winds more than in the nonturbulent simulations (Fig. 8b). In the nonturbulent simulations, the PPGF and Coriolis are nearly balanced above approximately 200 m AGL (cf. solid lines with dotted black line in Fig. 8a). Between about 100–200 m, both subgrid-scale and resolved mixing are instantaneously acting to weaken the shear in this layer by increasing the meridional winds from 50 to 100 m and decreasing them above (Fig. 8b). The PPGF counters these tendencies in order to maintain the wind profile (and thus the shear) in this layer (Fig. 8a).

Otherwise, the fact that the differences are relatively minor between the turbulent and non-turbulent-BL simulations can be explained by the overall small forcing from the TKE (either resolved or subgrid) on the wind profile above the shallow surface layer and the fact that the surface layer is completely dominated by the

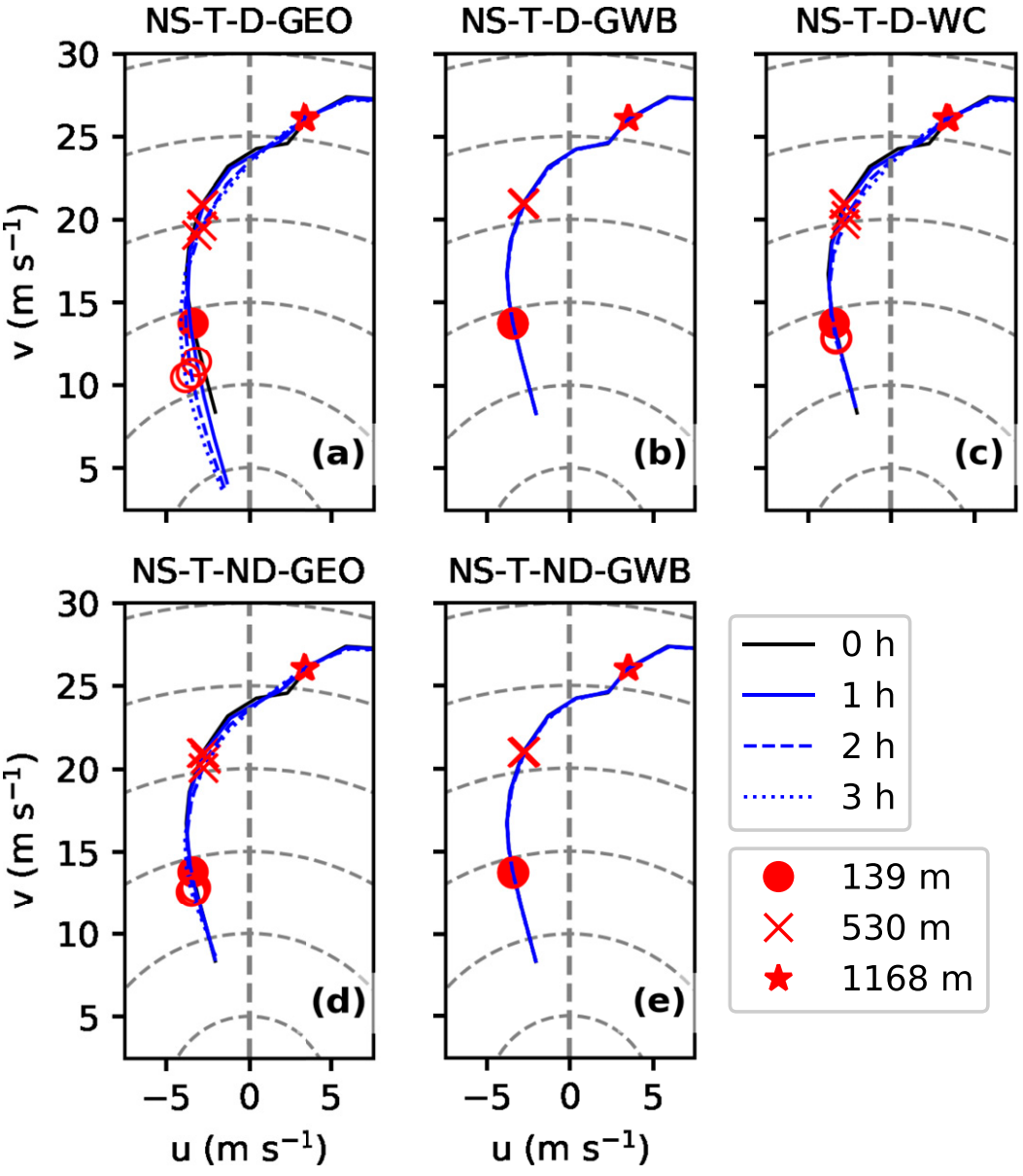

FIG. 7. As in Fig. 2, but for the no-storm simulations with turbulent boundary layer (NS-T-) runs.

subgrid-scale TKE, as seen in other LES-type simulations with similar resolutions (see Markowski and Bryan 2016, and references therein). We think it is plausible, however, that different wind profiles may exhibit somewhat different sensitivities, particularly when considering the effects of the thermodynamic profile. For example, turbulence would be enhanced for large virtual temperature lapse rates and suppressed for small lapse rates.

Finally, we also performed a series of storm experiments–analogous to the S-NT- experiments–but with a turbulent boundary layer (the S-T- experiments). The initialization of these simulations as well as the application of the GWB method is somewhat more complicated than in the corresponding S-NT- simulations. We desire to initiate storms in an environment where the boundary layer already has appreciable resolved turbulent structures. Therefore, we took the model output valid at 2 h from the no-storm GWB simulations (NS-T-D-GWB and NS-T-ND-GWB) and used them as the initial conditions for the appropriate sets of storm simulations (i.e., with and without surface drag, respectively). Since as already discussed the GWB method ensured that the average wind profile was preserved in NS-T-D-GWB and NS-T-ND-GWB, this means that the new set of S-T- simulations all start with the same *average* environmental wind profile as

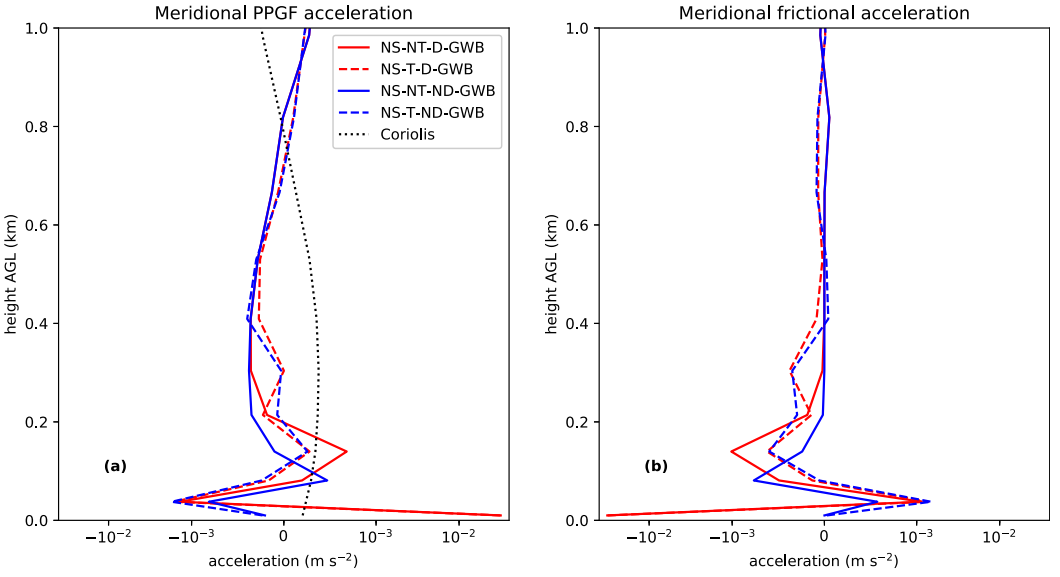

FIG. 8. Vertical profiles of the meridional component of (a) the PPGF acceleration and (b) the frictional force for the four no-storm GWB experiments. Red and blue curves indicate the experiments with and without surface drag, respectively. Solid and dashed curves are for the experiments without and with resolved BL turbulence, respectively. For the resolved-BL-turbulence experiments, the PPGF profile is shown for a model time of 2 h. The profile of the average Coriolis force (which is nearly identical between the four experiments since it depends only on the nearly constant vertical wind profile) is also shown (blacked dotted line) for reference in (a). Note the symmetric logarithmic scale for the abscissa.

those storm simulations *without* resolved BL turbulence (i.e., the S-NT- simulations). This approach is very similar to that of Nowotarski et al. (2015) who likewise initialized their supercell storm simulations from a previous set of simulations of convective boundary layers with fully developed turbulence. In their simulations, however, it was difficult to maintain the average low-level vertical wind profile over the course of their storm simulations because of the lack of a large-scale PGF to balance the turbulent mixing (Nowotarski et al. 2014); the GWB method provides this as follows. Recall that the PPGF profile was continuously updated for the two no-storm GWB experiments (NS-T-D-GWB and NS-T-ND-GWB), such that the average wind profile remained constant even while the boundary layer turbulence continuously evolved (cf. Fig. 5). For the two GWB storm experiments (S-T-D-GWB and S-T-ND-GWB) we used the PPGF profile valid at 2 h in NS-T-D-GWB and NS-T-ND-GWB, respectively, and then *held it fixed* for the duration of the two storm simulations. This ensures that in the horizontal mean, the PPGF profile balances the frictional force profile *at least at the initial time*. While we could have continued to update the PPGF profile in the face of the changing horizontal average of the horizontal momentum time-tendencies, as in the NS-T- experiments, in this case we would have been also compensating for the average of the *storm-induced perturbations* to the wind profile, which is undesirable for the present purposes. We show the wind profile evolution for the S-T- experiments in Fig. 9. Here, as in the storm simulations without resolved turbulence (the S-NT- experiments), the profiles are taken as a horizontal average of a $20 \times 20\,\text{km}^2$ area at the southeast corner of the inner 250-m mesh, to represent the far-inflow region (the $20 \times 20\,\text{km}^2$ is sufficient to average out the effects of the resolved turbulence, not shown). The same basic evolution is seen when comparing the hodographs between pairs of experiments from the NS-T- (Fig. 7) and S-T- (Fig. 9) sets indicating that the presence of the storm does not substantially affect the far-inflow wind profile, and that the GWB method reliably maintains it.

4. Impact of surface drag on simulated storm structure

Finally, motivated by the aforementioned recent work on this problem, we turn to a brief analysis of the impact of surface drag on simulated near-surface storm structure and behavior. As noted earlier, each simulation produced several intense tornado-strength vortices, with an overall increase in activity after ~2 h (cf. Fig. 3). As an initial foray, we wish to reveal any obvious differences in near-surface kinematic structure that persist over time across the simulations, since the near-surface wind field associated with the storm and attendant

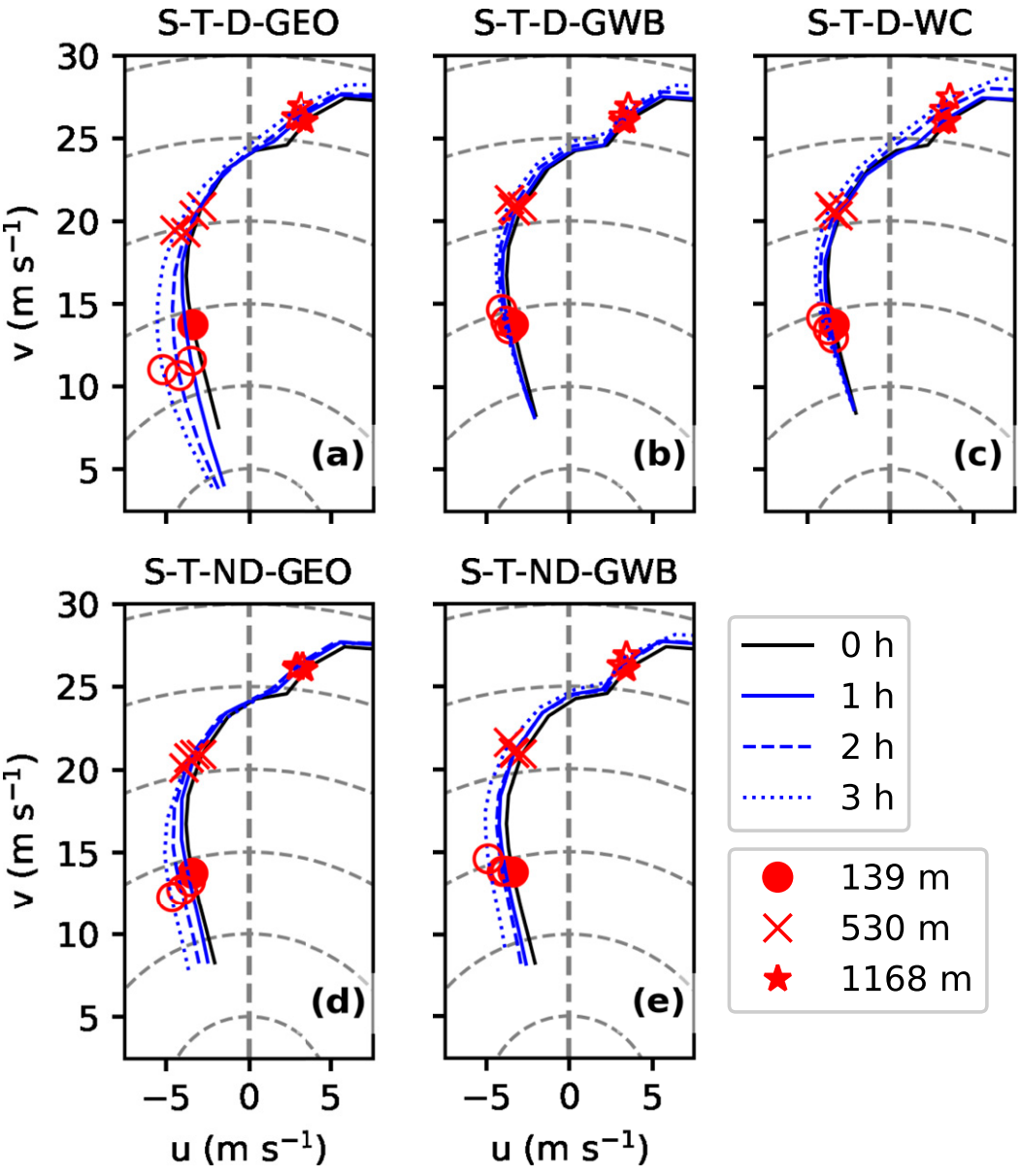

FIG. 9. As in Fig. 7, but for the storm simulations with turbulent boundary layer (S-T-) runs.

tornadoes would be expected to be most *directly* affected by the presence or absence of surface drag. To this end, we constructed temporal composites by tracking the location of maximum vertical vorticity within a $12 \times 12\,\text{km}^2$ moving box at 500 m AGL every 60 s during the second hour of each simulation and rejecting those times when the vertical vorticity decreased below $0.1\,\text{s}^{-1}$. Additionally, we rejected those times when the position of the vortex deviated more than 3 km from its median position of all the previous times; we found this to be necessary to avoid centering on spurious nontornadic or vortices that had significant storm-relative rearward motion (i.e., "occluding" vortices). We then aligned the model fields in the horizontal at the individual times relative to the surface vortex location and performed a simple average across the times.

We show the resulting composites for surface horizontal wind speed (color fill), asymptotic contraction rate (ACR; green contours),[1] and surface simulated

[1] This purely kinematic quantity is a measure of the long-term rate at which adjacent air parcels approach each other given a steady kinematic flow field, and is more useful for identifying airstream boundaries than simple divergence (Cohen and Schultz 2005; Betten et al. 2018).

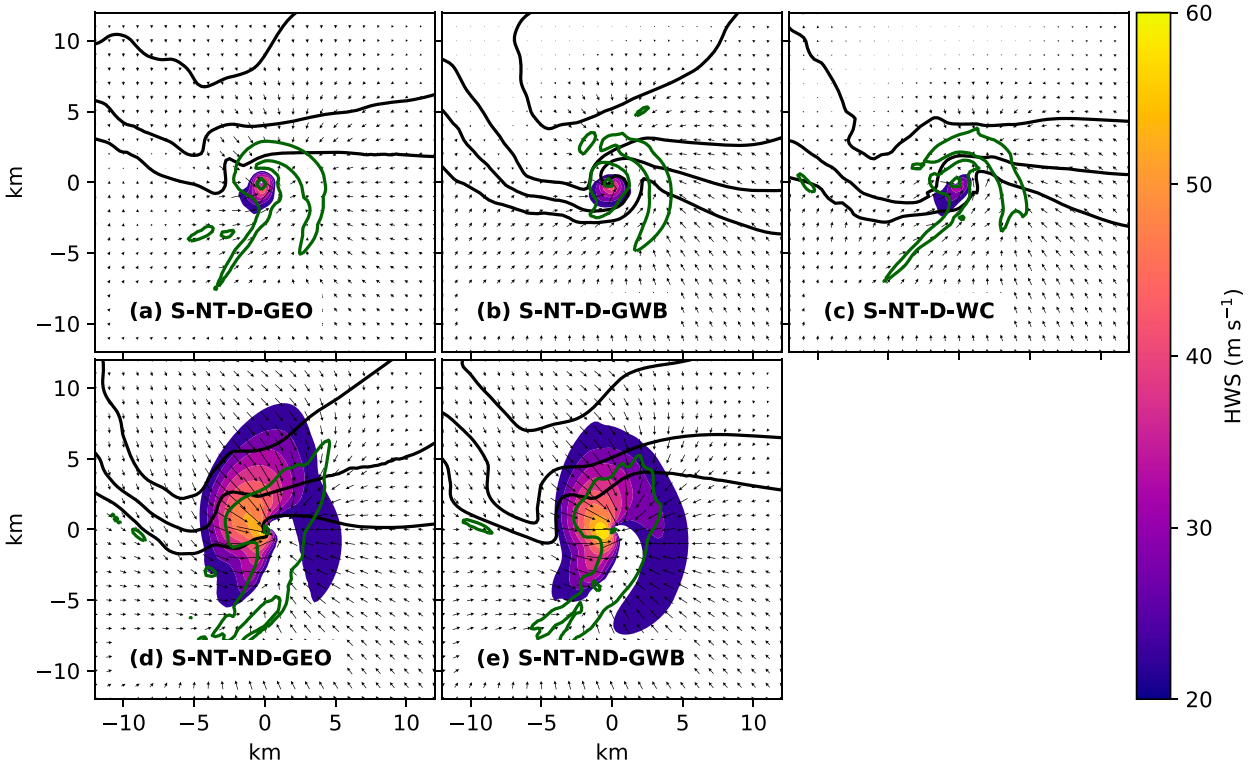

FIG. 10. Temporal composites (see text for details on the construction of the composites) centered on the location of maximum surface vorticity for each of the S-NT- runs. Shown in each composite is ground-relative surface wind speed (HWS; color fill, $m\,s^{-1}$), surface asymptotic contraction rate (ACR; green contour; $0.0075\,s^{-1}$ shown), and radar reflectivity (black contours, 10 dBZ increment, starting at 20 dBZ).

radar reflectivity (dBZ; black contours) in Fig. 10. While we performed these composites for both the S-NT- and S-T- sets of experiments, the results were not substantially different in a qualitative sense, and thus we show only the S-NT- results for the sake of brevity. The presence or absence of surface drag profoundly alters the near-surface kinematic structure of the storm. First, the two experiments without surface drag (S-NT-ND-GEO and S-NT-ND-GWB; Figs. 10d and 10e) exhibit a large area of strong surface winds $>20\,m\,s^{-1}$ up to 10 km from the vortex. In contrast, the three experiments with surface drag (S-NT-D-GEO, S-NT-D-GWB, and S-NT-D-WC; Figs. 10a–c) all show the strongest winds in a much smaller area close to the simulated tornado.

The two simulations without surface drag also exhibit a much more prominent rear-flank gust front (RFGF) as well as a prominent boundary extending off to the northeast of the surface vortex into the forward flank of the storm that resembles the "left flank convergence boundary" (LFCB) identified in the simulations of Beck and Weiss (2013). In contrast, the simulations with surface drag have a less prominent boundary in the mean in the forward flank region. Moreover, the structure of the RFGF and its orientation relative to the surface vortex is quite different between the simulations with and without surface drag. In the no-drag simulations, the RFGF appears as a single entity (at least in the mean, as defined by the compositing procedure) that appears nearly contiguous with the LFCB/FFGF, both having a roughly SSW to NNE orientation (green contours in Figs. 10d and 10e). The simulated tornado in these simulations is located very near the intersection of these two boundaries with less arcing of the RFGF. This structure is qualitatively similar to that seen in several other published simulations of supercells that used free-slip lower boundary conditions (e.g., Adlerman and Droegemeier 2002; Dahl et al. 2012; Beck and Weiss 2013). In contrast, in each of the three drag simulations, the RFGF forms a tightening cyclonic arc or spiral through at least 180°, that wraps around the simulated tornado such that the latter is "tucked" into the tighter, western portion of the spiral or even kinematically "detached" from it (green contours in Figs. 10a–c). Except for perhaps S-NT-D-GWB, there is little evidence for a prominent forward flank boundary in the mean, although inspection of individual times (especially later in the simulation) indicates that the drag simulations do form

several transient forward flank boundaries (not shown). This general forward- and rear-flank boundary structure is consistent with that found in several recent published simulations that included surface drag parameterizations (e.g., Schenkman et al. 2014, 2016; Dawson et al. 2015; Roberts et al. 2016; Coffer and Parker 2017; Coffer et al. 2017) and in observation-based studies (e.g., Skinner et al. 2011; Lee et al. 2012; Marquis et al. 2012; Kosiba et al. 2013; Skinner et al. 2014). Additionally, the drag experiments all show another persistent boundary trailing SSW from the vortex itself. This boundary is roughly parallel with the eastern portion of the RFGF and separated from it by ~5 km, and bears striking resemblance to the so-called secondary rear flank gust front or internal momentum surge identified in several recent modeling and observational analysis studies of tornadic supercells (e.g., Skinner et al. 2011; Lee et al. 2012; Schenkman et al. 2016; Marquis et al. 2012; Kosiba et al. 2013; Skinner et al. 2014). While the no-drag simulations also exhibit these secondary gust fronts, they are much more transient and thus do not show up in the composite fields.

Figure 10 suggests that the overall kinematic structure of the storm at the surface, at least during times when the surface vortex is most intense, is not appreciably different between the GWB/WC and non-GWB simulations. However, the two experiments that used a PPGF that offset surface drag (S-NT-D-GWB and S-NT-D-WC) have stronger southeasterly flow in the inflow region and weaker northwesterly flow in the outflow region north of the surface vortex than is the case in the experiment that included both surface drag and assumed initial geostrophic balance via (2) (S-NT-D-GEO). This can be seen by comparing wind vectors in the corresponding regions in Figs. 10b and 10c with Fig. 10a). The weaker southeasterly inflow into the storm in S-NT-D-GEO is clearly due to the surface drag weakening the near-surface flow (cf. hodograph Fig. 4a). The stronger environmental or background southeasterly flow in S-NT-D-GWB and S-NT-D-WC apparently cancel out some of the northwesterly storm-induced outflow northwest of the low-level vortex center to produce weaker total ground relative winds there (cf. wind vectors in the upper-left quadrant of Figs. 10b and 10c with Fig. 10a). Additionally, the winds in the composite vortex in S-NT-D-WC (color filled region in Fig. 10c) are noticeably weaker than in the other two drag simulations (Figs. 10a,b); this is also evident in the time series of maximum horizontal wind speed (Fig. 3, blue line). The reason for this difference is unclear, but may be related to the somewhat weaker shear that develops with time in the lowest ~500 m in the far-field inflow wind profile for this experiment (Fig. 4c, circle and × markers) as compared to S-NT-D-GEO and S-NT-D-GWB (Figs. 4a and 4b, respectively). A complete investigation into the reasons for these differences and a thorough comparison with previous simulations and observations is beyond the scope of this study but will be pursued in future work.

5. Summary and discussion

We have developed a new method to compute a large-scale pressure gradient for use within atmospheric simulation models with idealized background environments. The method is particularly useful for idealized simulations of convection and other phenomena where it is desirable to precisely control and maintain the large-scale kinematic environment while simultaneously including the effects of friction. A prime example are high-resolution supercell tornado simulations initialized from a single environmental sounding where satisfying both of these conditions has historically proven difficult. This difficulty arises due to the tendency for surface friction in particular to modify the low-level environmental wind profile over time if the large-scale PGF is not calculated appropriately to account for the frictional force in the large-scale force balance. The primary appeal of the new method is its applicability to an arbitrary wind profile coupled with any given surface drag and turbulence formulation, including in the presence of resolved turbulent structures that evolve over time. The method is conceptually simple and easy to implement in existing models, and works by determining the horizontal force as a function of height that is needed to cancel out the horizontal frictional and Coriolis forces. The method estimates this force profile as the negation of the time tendency of the horizontal momentum equations early in the simulation at each grid level in a suitable (i.e., perturbation free) column (or average of columns). This vertical force profile is then included as an additional term in the horizontal momentum equations for the duration of the simulation.

We demonstrated the method by applying it to a series of idealized simulations of a supercell using a sounding representative of the inflow environment of the storms in the 24 May 2011 Oklahoma tornado outbreak. With the Geotriptic Wind Balance method, the far-field low-level wind profile remains essentially unchanged throughout the 3–4 h model integration, even with the presence of surface drag and/or resolved turbulent eddies. The simulations with resolved boundary layer turbulent eddies were (somewhat surprisingly) very similar in their overall behavior with their non-turbulent counterparts, though subtle differences in the

evolution of the wind profiles did exist. Namely, there was a tendency for slightly more modification of the wind profile to occur over time when comparing corresponding experiments in the turbulent versus the nonturbulent boundary layer sets in which the GWB method was not employed. In ongoing work we are investigating the sensitivity of simulated supercells and their attendant tornadoes to the presence of surface drag and resolved versus subgrid-scale turbulence; as part of this effort we will continue to assess the utility of the GWB method for other wind profiles and higher grid resolutions in which turbulent structures would be better resolved. Results of these investigations will be reported in a future paper.

While in this study we focused on the goal of controlling (via maintaining) a *fixed* background wind profile, the emphasis should be on the word ''control'' rather than ''fixed''. The GWB method can easily be generalized to control other aspects of the environmental evolution, and has similarity to some methods found in the published literature. Nolan and Rappin (2008) applied a forcing term to the model horizontal momentum equations to maintain a time-invariant background vertical wind profile in order to investigate the effects of vertical wind shear in idealized simulations of tropical cyclones. Bryan et al. (2017) applied a similar method to maintain a time-invariant background flow that was in gradient wind balance in limited-area LES experiments to explore the wind profile in the tropical cyclone boundary layer. That is, they explicitly computed the required PPGF that would satisfy *gradient* wind balance rather than *geostrophic* as is more commonly used, and added this term to the model momentum equations in much the same manner as in the present study.

Other researchers have sought to examine in a controlled manner the impact of a *changing* background wind profile on simulated convective storm evolution. Letkewicz et al. (2013) used a method they dubbed ''base-state substitution'' where a simulation was performed with one kinematic and thermodynamic profile defining the horizontally homogeneous base state, which was then replaced with another at some time during the simulation. A limitation of this approach is seemingly the abrupt nature in which the background profile changes. Using an approach more similar to our own, Kost and Richardson (2004) applied a time-varying force profile to the momentum equations that slowly modified the background wind profile from one state to another with stronger wind shear. Our method can easily be modified to perform this function while simultaneously including the effects of surface friction. Another potential application in this vein would be for studying the effects of changing surface roughness within a single simulation, by interpolating over a short period the PPGF profiles that balance the frictional forces associated with two or more different values of the drag coefficient that are ''activated'' at specific times in the simulation. Furthermore, our method is not limited to convective storm or tropical cyclone simulations; it can be applied to, for example, idealized orographic flow simulations that include surface frictional effects. The same procedure can be used to help maintain the upstream wind profile that eventually flows over the mountain.

Acknowledgments. The authors wish to thank Dr. Chris Nowotarski and two other anonymous reviewers for their comments, which greatly improved the quality of the manuscript. We are grateful for the many fruitful discussions with colleagues regarding this work, including Drs. Johannes Dahl, Paul Markowski, Yvette Richardson, Lou Wicker, Ted Mansell, George Bryan, Brice Coffer, Patrick Skinner, Robin Tanamachi, and Corey Potvin, among many others. We also acknowledge Dr. George Bryan for his continued support of the CM1 model. Most of the postprocessing and plotting of the simulation output was carried out using the Python programming language and leveraged numerous open-source modules, most notably the MetPy (May et al. 2017) and matplotlib (Hunter 2007) packages. Support for this work came from the first author's institution in the form of start-up funding.

REFERENCES

Adlerman, E. J., and K. K. Droegemeier, 2002: The sensitivity of numerically simulated cyclic mesocyclogenesis to variations in model physical and computational parameters. *Mon. Wea. Rev.*, **130**, 2671–2691, https://doi.org/10.1175/1520-0493(2002)130<2671:TSONSC>2.0.CO;2.

Beck, J. R., and C. C. Weiss, 2013: An assessment of low-level baroclinity and vorticity within a simulated supercell. *Mon. Wea. Rev.*, **141**, 649–669, https://doi.org/10.1175/MWR-D-11-00115.1.

Betten, D. P., M. I. Biggerstaff, and C. L. Ziegler, 2018: Three-dimensional storm structure and low-level boundaries at different stages of cyclic mesocyclone evolution in a high-precipitation tornadic supercell. *Adv. Meteorology*, 2018, 9432670, https://doi.org/10.1155/2018/9432670.

Bryan, G. H., and J. M. Fritsch, 2002: A benchmark simulation for moist nonhydrostatic numerical models. *Mon. Wea. Rev.*, **130**, 2917–2928, https://doi.org/10.1175/1520-0493(2002)130<2917:ABSFMN>2.0.CO;2.

——, R. P. Worsnop, J. K. Lundquist, and J. A. Zhang, 2017: A simple method for simulating wind profiles in the boundary layer of tropical cyclones. *Bound.-Layer Meteor.*, **162**, 475–502, https://doi.org/10.1007/s10546-016-0207-0.

Coffer, B. E., and M. D. Parker, 2017: Simulated supercells in nontornadic and tornadic VORTEX2 environments.

Mon. Wea. Rev., **145**, 149–180, https://doi.org/10.1175/MWR-D-16-0226.1.

——, ——, J. M. L. Dahl, L. J. Wicker, and A. J. Clark, 2017: Volatility of tornadogenesis: An ensemble of simulated nontornadic and tornadic supercells in VORTEX2 environments. *Mon. Wea. Rev.*, **145**, 4605–4625, https://doi.org/10.1175/MWR-D-17-0152.1.

Cohen, R. A., and D. M. Schultz, 2005: Contraction rate and its relationship to frontogenesis, the Lyapunov exponent, fluid trapping, and airstream boundaries. *Mon. Wea. Rev.*, **133**, 1353–1369, https://doi.org/10.1175/MWR2922.1.

Dahl, J. M. L., M. D. Parker, and L. J. Wicker, 2012: Uncertainties in trajectory calculations within near-surface mesocyclones of simulated supercells. *Mon. Wea. Rev.*, **140**, 2959–2966, https://doi.org/10.1175/MWR-D-12-00131.1.

Davies-Jones, R. P., 2014: A review of supercell and tornado dynamics. *Atmos. Res.*, **158–159**, 1–18, https://doi.org/10.1016/J.ATMOSRES.2014.04.007.

Dawson, D. T., E. R. Mansell, Y. Jung, L. J. Wicker, M. R. Kumjian, and M. Xue, 2014: Low-level Z_{DR} signatures in supercell forward flanks: The role of size sorting and melting of hail. *J. Atmos. Sci.*, **71**, 276–299, https://doi.org/10.1175/JAS-D-13-0118.1.

——, M. Xue, J. A. Milbrandt, and A. Shapiro, 2015: Sensitivity of real-data simulations of the 3 May 1999 Oklahoma City tornadic supercell and associated tornadoes to multimoment microphysics. Part I: Storm- and tornado-scale numerical forecasts. *Mon. Wea. Rev.*, **143**, 2241–2265, https://doi.org/10.1175/MWR-D-14-00279.1.

Deardorff, J. W., 1980: Stratocumulus-capped mixed layers derived from a three-dimensional model. *Bound.-Layer Meteor.*, **18**, 495–527, https://doi.org/10.1007/BF00119502.

Fiedler, B. H., and R. Rotunno, 1986: A theory for the maximum wind speeds in tornado-like vortices. *J. Atmos. Sci.*, **43**, 2328–2340, https://doi.org/10.1175/1520-0469(1986)043<2328:ATOTMW>2.0.CO;2.

Hunter, J. D., 2007: Matplotlib: A 2d graphics environment. *Comput. Sci. Eng.*, **9**, 90–95, https://doi.org/10.1109/MCSE.2007.55.

Johnson, W., Jr., 1966: The ''geotriptic wind.'' *Bull. Amer. Meteor. Soc.*, **47**, 982.

Klemp, J. B., and R. B. Wilhelmson, 1978: The simulation of three-dimensional convective storm dynamics. *J. Atmos. Sci.*, **35**, 1070–1096, https://doi.org/10.1175/1520-0469(1978)035<1070:TSOTDC>2.0.CO;2.

Kosiba, K., J. M. Wurman, Y. P. Richardson, P. M. Markowski, P. Robinson, and J. Marquis, 2013: Genesis of the Goshen County, Wyoming, tornado on 5 June 2009 during VORTEX2. *Mon. Wea. Rev.*, **141**, 1157–1181, https://doi.org/10.1175/MWR-D-12-00056.1.

Kost, J., and Y. P. Richardson, 2004: The influence of temporally-varying vertical wind shear on numerically simulated convective storms. *22nd Conf. on Severe Local Storms*, Hyannis, MA, Amer. Meteor. Soc., 9.2, https://ams.confex.com/ams/11aram22sls/techprogram/paper_81785.htm.

Lee, B. D., C. A. Finley, and C. D. Karstens, 2012: The Bowdle, South Dakota, cyclic tornadic supercell of 22 May 2010: Surface analysis of rear-flank downdraft evolution and multiple internal surges. *Mon. Wea. Rev.*, **140**, 3419–3441, https://doi.org/10.1175/MWR-D-11-00351.1.

Letkewicz, C. E., A. J. French, and M. D. Parker, 2013: Base-state substitution: An idealized modeling technique for approximating environmental variability. *Mon. Wea. Rev.*, **141**, 3062–3086, https://doi.org/10.1175/MWR-D-12-00200.1.

Lewellen, D. C., and W. S. Lewellen, 2007: Near-surface intensification of tornado vortices. *J. Atmos. Sci.*, **64**, 2176–2194, https://doi.org/10.1175/JAS3965.1.

Loftus, A. M., D. B. Weber, and C. A. Doswell, 2008: Parameterized mesoscale forcing mechanisms for initiating numerically simulated isolated multicellular convection. *Mon. Wea. Rev.*, **136**, 2408–2421, https://doi.org/10.1175/2007MWR2133.1.

Mansell, E. R., 2010: On sedimentation and advection in multimoment bulk microphysics. *J. Atmos. Sci.*, **67**, 3084–3094, https://doi.org/10.1175/2010JAS3341.1.

Markowski, P. M., 2016: An idealized numerical simulation investigation of the effects of surface drag on the development of near-surface vertical vorticity in supercell thunderstorms. *J. Atmos. Sci.*, **73**, 4349–4385, https://doi.org/10.1175/JAS-D-16-0150.1.

——, and G. H. Bryan, 2016: LES of laminar flow in the PBL: A potential problem for convective storm simulations. *Mon. Wea. Rev.*, **144**, 1841–1850, https://doi.org/10.1175/MWR-D-15-0439.1.

Marquis, J., Y. P. Richardson, P. M. Markowski, D. C. Dowell, and J. M. Wurman, 2012: Tornado maintenance investigated with high-resolution dual-Doppler and EnKF analysis. *Mon. Wea. Rev.*, **140**, 3–27, https://doi.org/10.1175/MWR-D-11-00025.1.

Mashiko, W., 2016: A numerical study of the 6 May 2012 Tsukuba City supercell tornado. Part II: Mechanisms of tornadogenesis. *Mon. Wea. Rev.*, **144**, 3077–3098, https://doi.org/10.1175/MWR-D-15-0122.1.

May, R., S. Arms, P. Marsh, E. Bruning, and J. Leeman, 2017: Metpy: A Python package for meteorological data. Unidata, Boulder, CO, accessed 25 September 2019, https://github.com/Unidata/MetPy, https://doi.org/10.5065/D6WW7G29.

Muñoz-Esparza, D., B. Kosović, J. Mirocha, and J. van Beeck, 2014: Bridging the transition from mesoscale to microscale turbulence in numerical weather prediction models. *Bound.-Layer Meteor.*, **153**, 409–440, https://doi.org/10.1007/s10546-014-9956-9.

Naylor, J., and M. S. Gilmore, 2012: Convective initiation in an idealized cloud model using an updraft nudging technique. *Mon. Wea. Rev.*, **140**, 3699–3705, https://doi.org/10.1175/MWR-D-12-00163.1.

Nolan, D. S., and E. D. Rappin, 2008: Increased sensitivity of tropical cyclogenesis to wind shear in higher SST environments. *Geophys. Res. Lett.*, **35**, 1–7, https://doi.org/10.1029/2008GL034147.

Nowotarski, C. J., P. M. Markowski, Y. P. Richardson, and G. H. Bryan, 2014: Properties of a simulated convective boundary layer in an idealized supercell thunderstorm environment. *Mon. Wea. Rev.*, **142**, 3955–3976, https://doi.org/10.1175/MWR-D-13-00349.1.

——, ——, ——, and ——, 2015: Supercell low-level mesocyclones in simulations with a sheared convective boundary layer. *Mon. Wea. Rev.*, **143**, 272–297, https://doi.org/10.1175/MWR-D-14-00151.1.

Orf, L., R. Wilhelmson, B. Lee, C. Finley, and A. Houston, 2017: Evolution of a long-track violent tornado within a simulated supercell. *Bull. Amer. Meteor. Soc.*, **98**, 45–68, https://doi.org/10.1175/BAMS-D-15-00073.1.

Parker, M. D., 2014: Composite VORTEX2 supercell environments from near-storm soundings. *Mon. Wea. Rev.*, **142**, 508–529, https://doi.org/10.1175/MWR-D-13-00167.1.

Roberts, B., and M. Xue, 2017: The role of surface drag in mesocyclone intensification leading to tornadogenesis within an idealized supercell simulation. *J. Atmos. Sci.*, **74**, 3055–3077, https://doi.org/10.1175/JAS-D-16-0364.1.

——, ——, A. D. Schenkman, and D. T. Dawson, 2016: The role of surface drag in tornadogenesis within an idealized supercell simulation. *J. Atmos. Sci.*, **73**, 3371–3395, https://doi.org/10.1175/JAS-D-15-0332.1.

Schenkman, A. D., M. Xue, and M. Hu, 2014: Tornadogenesis in a high-resolution simulation of the 8 May 2003 Oklahoma City supercell. *J. Atmos. Sci.*, **71**, 130–154, https://doi.org/10.1175/JAS-D-13-073.1.

——, ——, and D. T. Dawson, 2016: The cause of internal outflow surges in a high-resolution simulation of the 8 May 2003 Oklahoma City tornadic supercell. *J. Atmos. Sci.*, **73**, 353–370, https://doi.org/10.1175/JAS-D-15-0112.1.

Skinner, P. S., C. C. Weiss, J. L. Schroeder, L. J. Wicker, and M. I. Biggerstaff, 2011: Observations of the surface boundary structure within the 23 May 2007 Perryton, Texas, supercell. *Mon. Wea. Rev.*, **139**, 3730–3749, https://doi.org/10.1175/MWR-D-10-05078.1.

——, ——, M. M. French, H. B. Bluestein, P. M. Markowski, and Y. P. Richardson, 2014: VORTEX2 observations of a low-level mesocyclone with multiple internal rear-flank downdraft momentum surges in the 18 May 2010 Dumas, Texas, supercell. *Mon. Wea. Rev.*, **142**, 2935–2960, https://doi.org/10.1175/MWR-D-13-00240.1.

Wicker, L. J., and R. B. Wilhelmson, 1993: Numerical simulation of tornadogenesis within a supercell thunderstorm. *The Tornado: Its Structure, Dynamics, Prediction, and Hazards*, *Geophys. Monogr.*, Vol. 79, Amer. Geophys. Union, 75–88.

Wilhelmson, R. B., and C.-S. Chen, 1982: A simulation of the development of successive cells along a cold outflow boundary. *J. Atmos. Sci.*, **39**, 1466–1483, https://doi.org/10.1175/1520-0469(1982)039<1466:ASOTDO>2.0.CO;2.